Transition of the scaling law in inverse energy cascade range caused by a nonlocal excitation of coherent structures observed in two-dimensional turbulent fields

Atsushi Mizuta[*]

Software Cradle Co., Ltd., 3-4-5, Umeda, Kita-ku Osaka, Japan and Division of Physics and Astronomy, Graduate School of Science, Kyoto University, Kyoto 606-8502, Japan

Takeshi Matsumoto and Sadayoshi Toh

Division of Physics and Astronomy, Graduate School of Science, Kyoto University, Kyoto 606-8502, Japan

We numerically investigate the inverse energy cascade range of two-dimensional Navier-Stokes turbulence. Our focus is on the universality of the Kolmogorov's phenomenology. In our direct numerical simulations, two types of forcing processes, the random forcing and the deterministic forcing, are employed besides the systematically varied numerical parameters. We first calculate the two-dimensional Navier-Stokes equations and confirm that results in the quasi steady state are consistent with the classical phenomenology for both types of forcing processes. It is also found that the difference in forcing process appears after the inverse energy cascade range reaches the system size; the dipole coherent vortices emerge and grow only when the random forcing is adopted. Then we add a large-scale drag term to the Navier-Stokes equations to obtain the statistically stationary state. When the random forcing is used, the scaling exponent of the energy spectrum in the stationary state starts to differ from the predicted $-5/3$ in the inverse energy cascade range as the infrared Reynolds number Re_d increases, where Re_d is defined as k_f/k_d with the forcing wave number k_f and the large-scale drag wave number k_d. That can be interpreted as a transition phenomenon in which the local maximum vorticity grows like an order parameter caused by excitation of strong coherent vortices. Strong coherent vortices emerge and grow after the quasi steady state and destroy the scaling law when Re_d is over a critical value. These coherent vortices are not due to the finite-size effect, unlike the dipole coherent vortices. On the other hand, when the deterministic forcing is adopted, strong coherent vortices are hardly seen and the $-5/3$ scaling law holds independently of Re_d. We examine the cases of the combination of both types of forcing processes and find that formation of such coherent vortices is sensitive to the mechanism of the external forcing process as well as the numerical parameters. Several types of large-scale drag terms are also tested and their insignificant influence on these qualitative properties is revealed.

I. INTRODUCTION

One of the most important achievements in two-dimensional Navier-Stokes turbulence studies is the Kraichnan-Leith-Batchelor (KLB) theory developed in Refs. [1–3]. In this theory, Kolmogorov's phenomenology for three-dimensional turbulence is applied to homogeneous, isotropic, and statistically (quasi-)stationary two-dimensional forced turbulence. As the vorticity of each fluid parcel is conserved in the inviscid case, both energy and enstrophy are inviscid invariants in the two-dimensional system. Under these two constraints, Kraichnan [1], based on Fjørtoft's work [4], first predicted the existence of two different scaling ranges: the inverse energy cascade range, where energy, injected by external forcing at intermediate scales, transfers to ever larger scales, and the direct enstrophy cascade range, where injected enstrophy transfers from forcing scales to smaller scales. From dimensional analysis, $k^{-5/3}$ and k^{-3} (with a possible logarithmic correction [5]) scaling laws are predicted for the energy spectrum in the inertial subranges of both inverse and direct cascade ranges, respectively.

To verify the KLB theory, many theoretical and mathematical analyses [6–14], numerical simulations [9,15–39], and laboratory experiments [29,30,40–42] have been performed. These theoretical and mathematical works primarily consider constraints on the forcing to be consistent with the KLB dual cascade picture. For typical classes of the deterministic forcings, by assuming that a statistically steady state is reached, such constraints are obtained, outside of which the energy spectrum differs from $k^{-5/3}$ and k^{-3} separated by the forcing wave number [6,8]. However, one must bear in mind that the assumption of the statistical steadiness is not made in the original KLB argument. In the random forcing cases [7,13,14], moments of the vorticity and the invariant measure has been studied as well as the constraints. To our knowledge, theoretical comparison between the two types of forcing is not very common, perhaps due to difference of the theoretical and mathematical tools. In this paper, we do this comparison numerically.

In the above-mentioned previous simulations and experiments, the $k^{-5/3}$ scaling [16,18,20,22,23,28,30,33,34,40,41] and the k^{-3} scaling [19,26,27,35] have been confirmed independently. Recently, both scaling laws have also simultaneously observed in laboratory experiments [29,42] and numerical simulations [32,36,38], even though the scaling ranges cannot be so wide in such studies. In Refs. [32,36], the k^{-3} scaling is asymptotically achieved as the Reynolds number increases.

However, the departure from the $k^{-5/3}$ scaling in the inverse energy cascade range is also recognized in some

───────────
[*]atsushi@kyoryu.scphys.kyoto-u.ac.jp

numerical studies [9,20–22,24,25,31,37,39]. In such cases, strong coherent vortices are usually observed in vorticity field and they are supposed to be the cause of this departure [20–22,24,25,31,37,39]. The mechanism of the formation of such coherent vortices has not been well understood and there seems to be no general agreement on the conditions for emergence of these strong coherent vortices. It is stated in Refs. [31,37,39] that when the direct enstrophy cascade range is well resolved, strong coherent vortices emerge and the $k^{-5/3}$ scaling is destroyed. On the other hand, the $k^{-5/3}$ scaling is obtained with a relatively wide direct enstrophy cascade range in Refs. [32,36]. It is also demonstrated in Refs. [37] that high resolution in the inverse energy cascade range causes the emergence of strong coherent vortices. In Ref. [22], the importance of employing the appropriate large-scale drag formulation to obtain the statistically stationary structureless turbulent flow field that holds the $k^{-5/3}$ energy spectrum is illustrated by using a specially devised large-scale drag. Nevertheless, relatively wide $k^{-5/3}$ scaling range is achieved with a hypodrag term in Ref. [34].

The KLB theory outlines the universal features which should be independent of the details of energy input and output mechanism. Under circumstances where a lot of data supports the KLB theory, it has been usual to adopt only one type of forcing process in each previous numerical study. However, previous numerical simulation results imply that the formation of strong coherent vortices, which causes the departure from the $k^{-5/3}$ scaling law, is not a universal phenomenon. Thus, it should be tested if the forcing mechanism can influence on the formation of coherent vortices and the $k^{-5/3}$ scaling law, and, if so, how it does. The fact that the type of forcing process modifies the slope of scaling in the enstrophy inertial subrange was shown in Ref. [38]. In this study, we use two typical types of forcing process. In each case, we investigate the conditions for formation of strong coherent vortices and the departure of the $k^{-5/3}$ scaling law by varying numerical parameters to mainly control the resolution in the inverse energy cascade range. We will show that formation of strong coherent vortices can be described as a transition phenomenon for the change in the numerical resolution in the inverse energy cascade range and that highly depends on the type of forcing process.

As is usual with numerical studies of two-dimensional Navier-Stokes turbulence, a large-scale drag term is added to the Navier-Stokes equations in this study to dissipate the energy transferred from the forcing scale and attain a statistically stationary state. However, this additional term of course can influence statistical features not only in large scales but also in the inverse energy cascade range. To see the influence of the drag term, the Navier-Stokes equations (without any large-scale drag term) are also calculated in this study. It is reported in Refs. [18,20,33] that strong dipole coherent vortices emerge and grow after the inverse energy cascade range reaches the system size when no drag term is added. We reproduce this dipole structure and compare it with the coherent structures observed when a large-scale drag term is added. We also employ several types of large-scale drag terms to check the influence of them.

The rest of this paper is organized as follows. In Sec. II, we show our numerical method and parameters. The numerical results are presented and discussed in Sec. III. The results for

two types of forcing processes without any large-scale drag terms are shown in Sec. III A. A statistically stationary state is attained for both types of forcing processes by adding the first-order hypodrag term in Sec. III B. Statistical features in such states with various numerical parameters are shown in this subsection. To see the effect of the forcing processes, a combination of two types of forcing processes is examined in Sec. III C. Several types of large-scale drag terms are also tested in Sec. III D. Section IV contains a brief discussion of the results in Sec. III and conclusions.

II. NUMERICAL METHOD

In our direct numerical simulation study, the two-dimensional Navier-Stokes equations are solved by using the pseudospectral method with the 2/3 dealiasing rule in a doubly periodic square domain of each side length 2π. The fourth-order Runge-Kutta method is employed for time integration. In practice, the vorticity equation in Fourier space,

$$\frac{\partial \hat{\omega}(\boldsymbol{k},t)}{\partial t} + [\widehat{(\boldsymbol{u} \cdot \boldsymbol{\nabla})\omega}](\boldsymbol{k},t)$$
$$= -(\nu k^{2h} + d k^{-2q})\hat{\omega}(\boldsymbol{k},t) + \hat{f}(\boldsymbol{k},t), \quad (1)$$

is integrated with the incompressible condition ($\boldsymbol{\nabla} \cdot \boldsymbol{u}(\boldsymbol{x},t) = 0$), where ˆ denotes the Fourier transform, $\boldsymbol{u}$ is the fluid velocity, $\omega \, (= -\boldsymbol{\nabla} \times \boldsymbol{u}|_z)$ the vorticity, ν the hyperviscosity coefficient, h the hyperviscosity exponent, d the hypodrag coefficient, q the hypodrag exponent, and f the forcing term. The large-scale drag term, the second term on the right-hand side of Eq. (1), is added to the Navier-Stokes equations in this study to dissipate the energy transferred from small forcing scales and obtain a statistically stationary turbulent flow field. Note that this term is dropped by reducing d to zero in Sec. III A to see the influence of it.

The forcing term is band-limited in Fourier space; the forcing wave range is $k_f - \Delta k \leqslant k \leqslant k_f + \Delta k$ for a small constant $\Delta k \, (< 0.01 k_f)$. As mentioned before, two types of forcing processes are employed in this study. One is the white-in-time random forcing process (here denoted as f_R for brevity), which is

$$\hat{f}(\boldsymbol{k},t)$$
$$= \begin{cases} \sqrt{\dfrac{\varepsilon_{\text{in}} k_f^2}{\Delta t \, n_f}} (\xi_{\boldsymbol{k}}^R + \mathrm{i}\xi_{\boldsymbol{k}}^I) & \text{if } |\boldsymbol{k}| \in [k_f - \Delta k, k_f + \Delta k], \\ 0 & \text{if } |\boldsymbol{k}| \notin [k_f - \Delta k, k_f + \Delta k], \end{cases}$$
$$\quad (2)$$

in Eq. (1). Here $\xi_{\boldsymbol{k}}^R$ and $\xi_{\boldsymbol{k}}^I$ are both independent, zero-mean, unit variance, Gaussian random variables which are independent for every $\boldsymbol{k}$ at every time step, Δt is a time step, and n_f is the number of the spectral modes in the forcing range. A control parameter ε_{in} is supposed to be an energy input rate. We have confirmed that the short-time averaged energy input rate is equal to ε_{in} from the results of the energy budget in each simulation. This type of forcing is widely used in the previous studies [16,18–22,26,31,37,39] and strong coherent vortices are formed in some cases. The other one is the deterministic

forcing process (here denoted as f_D), which is

$$\hat{f}(\boldsymbol{k},t) = \begin{cases} \frac{\varepsilon_{\mathrm{in}}|\boldsymbol{k}|^2}{n_f \, \hat{\omega}^*(\boldsymbol{k},t)} & \text{if } |\boldsymbol{k}| \in [k_f - \Delta k, k_f + \Delta k], \\ 0 & \text{if } |\boldsymbol{k}| \notin [k_f - \Delta k, k_f + \Delta k], \end{cases} \quad (3)$$

in Eq. (1). Here $\hat{\omega}^*$ denotes the complex conjugate of $\hat{\omega}$. With this forcing, a relatively wide $k^{-5/3}$ scaling range is achieved without coherent vortices in Ref. [34]. The same [27,30,34] and a similar type of forcing [9,28,43] are used in previous studies. The attractive aspect of this formulation is that it provides a constant energy input rate $\varepsilon_{\mathrm{in}}$ at every time step.

The initial condition is a homogeneous zero vorticity field when f_R is used. On the other hand, a random vorticity field with a small variance is prepared as an initial state when f_D is used, since the forcing term cannot be calculated when the vorticity is zero. This random vorticity field consists of Fourier modes generated with independent Gaussian distributions and scaled to give the energy spectrum

$$E(k,0) = \begin{cases} e_0 & \text{if } |\boldsymbol{k}| \leqslant k_f + \Delta k, \\ 0 & \text{if } |\boldsymbol{k}| > k_f + \Delta k, \end{cases} \quad (4)$$

for a small constant e_0 $(= 1.0 \times 10^{-8})$ as in Ref. [34]. Here the energy spectrum $E(k,t)$ is defined as

$$E(k,t) \equiv \frac{1}{\delta k} \sum_{k \leqslant |\boldsymbol{k}'| < k+\delta k} \frac{1}{2} |\hat{\boldsymbol{u}}(\boldsymbol{k}')|^2, \quad (5)$$

for small δk $(= 1)$.

Numerical parameters in our main simulations are listed in Table I. We employ 512^2, 1024^2, 2048^2, and 4096^2 for the number N^2 of spatial grid points in the calculation domain. While the energy input rate $\varepsilon_{\mathrm{in}}$ is fixed at 0.1, the forcing wave number k_f is set in proportion to N. To concentrate the computational resources on the inverse energy cascade range, the eighth-order hyperviscosity ($h = 8$) is used and the localized forcing scale is set in the vicinity of the viscous range. Consequently, the direct enstrophy cascade range is not resolved well.

The hyperviscosity coefficient ν is varied to obtain an approximately constant energy transfer rate $\varepsilon_{\mathrm{tr}}$ in these simulations. It is empirically found that to have almost the same $\varepsilon_{\mathrm{tr}}$ with fixed $\varepsilon_{\mathrm{in}}$, the viscous wave number k_ν defined as $(\varepsilon_{\mathrm{in}}/\nu^3)^{1/(6h-2)}$ should be proportional to k_f and N. We also use various numerical parameters for a large-scale drag term, d and q, to see the effect of the drag term; however, it is revealed that these parameters influence little on $\varepsilon_{\mathrm{tr}}$. Note that the ratio of energy transfer rate $\varepsilon_{\mathrm{tr}}$ to energy input rate $\varepsilon_{\mathrm{in}}$ is denoted as the inverse-cascade strength in Ref. [28] and treated as the key quantity to attain the k^{-3} scaling of energy spectrum in the enstrophy cascading range. It is also stated in Ref. [9,28] that the $k^{-5/3}$ inverse cascading range is realizable even for small $\varepsilon_{\mathrm{tr}}/\varepsilon_{\mathrm{in}}$. In all simulations shown in Table I, $\varepsilon_{\mathrm{tr}}/\varepsilon_{\mathrm{in}} = 0.18 \pm 0.01$.

III. RESULTS

A. Without any large-scale drag term

We begin with calculating the Navier-Stokes equations (without any large-scale drag term) to set a baseline for simulations with a large-scale drag term. On the basis of the KLB theory, there would be a quasi steady state [1], where

TABLE I. Numerical settings in each simulation are listed below: N^2 is the number of spatial grid points, f the type of forcing process, $\varepsilon_{\mathrm{in}}$ energy input rate, k_f the forcing wave number, h the hyperviscosity exponent, ν the hyperviscosity coefficient, q the hypodrag exponent, and d the hypodrag coefficient.

Name	N^2	f	$\varepsilon_{\mathrm{in}}$	k_f	h	ν	q	d
AR1	512^2	f_R	0.1	124	8	7.95×10^{-34}	—	0
AD1	512^2	f_D	0.1	124	8	7.95×10^{-34}	—	0
BR1	512^2	f_R	0.1	124	8	7.95×10^{-34}	1	0.2
BR2	512^2	f_R	0.1	124	8	7.95×10^{-34}	1	2.0
BR3	512^2	f_R	0.1	124	8	7.95×10^{-34}	1	2.5
BR4	512^2	f_R	0.1	124	8	7.95×10^{-34}	1	4.0
BR5	512^2	f_R	0.1	124	8	7.95×10^{-34}	1	5.0
BR6	512^2	f_R	0.1	124	8	7.95×10^{-34}	1	10
BD1	512^2	f_D	0.1	124	8	7.95×10^{-34}	1	0.2
BD2	512^2	f_D	0.1	124	8	7.95×10^{-34}	1	2.0
BD3	512^2	f_D	0.1	124	8	7.95×10^{-34}	1	10
CR1	1024^2	f_R	0.1	249	8	1.82×10^{-38}	1	2.5
CR2	1024^2	f_R	0.1	249	8	1.82×10^{-38}	1	7.5
CR3	1024^2	f_R	0.1	249	8	1.82×10^{-38}	1	25
CR4	1024^2	f_R	0.1	249	8	1.82×10^{-38}	1	30
CR5	1024^2	f_R	0.1	249	8	1.82×10^{-38}	1	35
DR1	2048^2	f_R	0.1	498	8	4.50×10^{-43}	1	50
DR2	2048^2	f_R	0.1	498	8	4.50×10^{-43}	1	100
DR3	2048^2	f_R	0.1	498	8	4.50×10^{-43}	1	150
DR4	2048^2	f_R	0.1	498	8	4.50×10^{-43}	1	175
DR5	2048^2	f_R	0.1	498	8	4.50×10^{-43}	1	180
DR6	2048^2	f_R	0.1	498	8	4.50×10^{-43}	1	190
DR7	2048^2	f_R	0.1	498	8	4.50×10^{-43}	1	200
ER1	4096^2	f_R	0.1	997	8	1.13×10^{-47}	1	2.0
ED1	4096^2	f_D	0.1	997	8	1.13×10^{-47}	1	2.0
FR1	512^2	f_R	0.1	124	8	7.95×10^{-34}	0	0.01
FR2	512^2	f_R	0.1	124	8	7.95×10^{-34}	0	0.02
FD1	512^2	f_D	0.1	124	8	7.95×10^{-34}	0	0.01
FD2	512^2	f_D	0.1	124	8	7.95×10^{-34}	0	0.02
GR1	2048^2	f_R	0.1	498	8	4.664×10^{-43}	0	0.02
GR2	2048^2	f_R	0.1	498	8	4.664×10^{-43}	0	0.05
GD1	2048^2	f_D	0.1	498	8	4.664×10^{-43}	0	0.02
HR1	512^2	f_R	0.1	124	8	7.95×10^{-34}	2	400
HR2	512^2	f_R	0.1	124	8	7.95×10^{-34}	2	750
HR3	512^2	f_R	0.1	124	8	7.95×10^{-34}	2	800
HD1	512^2	f_D	0.1	124	8	7.95×10^{-34}	2	750
ID1	2048^2	f_D	0.1	498	8	4.664×10^{-43}	2	20
JR1	512^2	f_R	0.1	124	8	7.95×10^{-34}	8	4.0×10^{14}
JR2	512^2	f_R	0.1	124	8	7.95×10^{-34}	8	6.0×10^{14}
JD1	512^2	f_D	0.1	124	8	7.95×10^{-34}	8	4.0×10^7
KD1	2048^2	f_D	0.1	498	8	4.664×10^{-43}	8	4.0×10^7

the scaling range called inertial subrange is observed, before the inverse energy cascade range reaches the system size. In the inertial subrange of inverse energy cascade range, energy should transfer scale-locally toward large scales at a constant rate $\varepsilon_{\mathrm{tr}}$ and the energy spectrum $E(k)$ should take the form

$$E(k) = C_K \varepsilon_{\mathrm{tr}}^{2/3} k^{-5/3}, \quad (6)$$

where C_K is the dimensionless universal constant called the Kolmogorov constant.

In this subsection, the results of AR1 and AD1 in Table I are presented. Two types of forcing processes, f_R and f_D, are used independently in each simulation. Time evolution of the
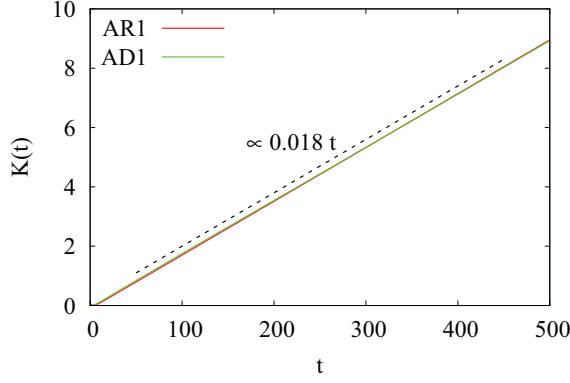
FIG. 1. (Color online) Time evolution of total kinetic energy in AR1 and AD1. Lines for AR1 and AD1 are indistinguishable due to overlap. Time scale $T_L(\equiv \varepsilon_{\rm in}^{-1/3}(2\pi)^{2/3})$ is about 7.3 in both cases.

total kinetic energy, defined as

$$K(t) \equiv \sum_{\bm{k}} \frac{1}{2}|\hat{\bm{u}}(\bm{k},t)|^2, \qquad (7)$$

is shown in Fig. 1. In both cases, the total kinetic energy grows linearly with time after the initial stage ($t \gtrsim T_L$), where the time scale T_L defined as $\varepsilon_{\rm in}^{-1/3}(2\pi)^{2/3}$ is 7.3. This linear growth of total kinetic energy, $K(t) \propto 0.018t$, is observed for a long time period, which is at least over $60T_L$.

The quasi steady state is observed in both cases in an intermediate time region, $T_L \lesssim t \lesssim 3T_L$. In this time region, the energy peak wave number k_p goes down toward lower wave numbers and the $k^{-5/3}$ energy spectrum is observed for $k_p \lesssim k \lesssim k_f$ as shown in Fig. 2.

The energy flux function, defined as

$$\Pi_E(k,t) \equiv \sum_{|\bm{k}'|<k} \frac{1}{|\bm{k}'|^2} {\rm Re}[\hat{\omega}^*(\bm{k}',t)\widehat{(\bm{u}\cdot\bm{\nabla})\omega}(\bm{k}',t)], \quad (8)$$

in this time region is also shown in Fig. 3. Energy conservation following the Navier-Stokes equations (with using hyperviscosity) is expressed with this function as follows:

$$\frac{\partial}{\partial t}\int_k^{\infty} E(k',t)dk' = \Pi_E(k,t)$$
$$- 2\nu\int_k^{\infty} k'^{2h}E(k',t)dk' + \int_k^{\infty} F(k',t)dk', \quad (9)$$
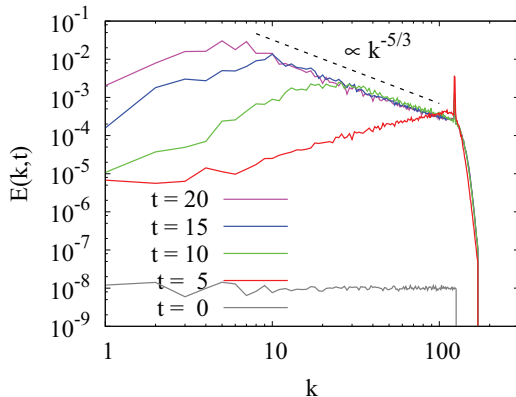
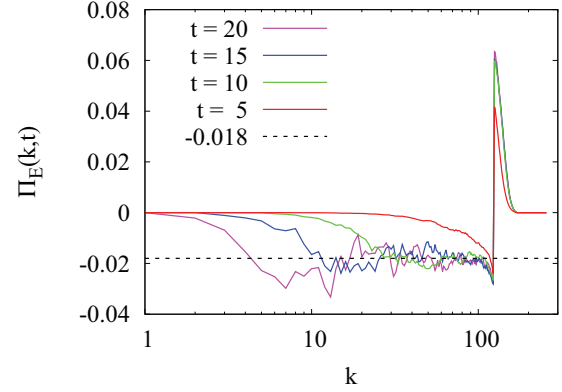FIG. 2. (Color online) Snapshots of energy spectrum at $t = 20, 15, 10, 5$, and 0 (from top to bottom) in AD1.

FIG. 3. (Color online) Snapshots of energy flux function at $t = 20, 15, 10$, and 5 (from left to right) in AD1.

where $F(k,t)$ is the energy input rate by the external forcing. Since $F(k,t)$ is nonzero only for $k_f - \Delta k \leqslant k \leqslant k_f + \Delta k$ and the value of $2\nu k^{2h}E(k,t)$ is very small for $k \ll k_f$, the growth rate of the kinetic energy at intermediate or large scales is estimated as follows:

$$\frac{\partial}{\partial t}\int_k^{k'} E(k'',t)dk'' \sim \Pi_E(k,t) - \Pi_E(k',t), \quad (10)$$

for $k < k' < k_f$. As shown in Fig. 3, $\Pi_E(k,t)$ gives a negative constant $-\varepsilon_{\rm tr}$ with some fluctuation in the $k^{-5/3}$ energy spectrum range. The constant value $\varepsilon_{\rm tr}$ is approximately 0.018 and obviously coincides with the growth rate of total kinetic energy.

These facts imply that only a small part of kinetic energy input by the external forcing is transferred at a constant rate $\varepsilon_{\rm tr}$ to large scales around the energy peak wave number k_p, which goes down toward lower wave numbers in time. Because of the closeness between the forcing range and the viscous range, the most part [~ 0.82 ($= 1 - \varepsilon_{\rm tr}/\varepsilon_{\rm in}$)] of injected energy is dissipated in the viscous range. In the original inverse energy cascade theory [1], most of the input energy supposed to be carried down toward the lower wave number; however, this cascading process observed in our simulations is qualitatively consistent with the theory. Almost the same results have been obtained in the previous numerical simulations [18,20]. There is no distinct difference in both cases, f_R and f_D, in the quasi steady state.

The difference between the results of f_R and f_D appears after the quasi steady state. Until the end of our simulation of the quasi steady state, the distribution of vorticity in physical space is structureless in the sense that the strong coherent vortices such as shown in Fig. 4 and Fig. 12 are not observed in both cases. When f_D is used, the vorticity field remains structureless, as demonstrated in Fig. 5 and Fig. 6, even when $t \sim 60T_L$, which is the end of the simulation time. On the other hand, when f_R is used, two coherent vortices of opposite sign illustrated in Fig. 4 and Fig. 6 get to be distinguishable at $t \sim 8T_L$, when the energy peak wave number reaches the fundamental mode ($k = 1$). The intensity
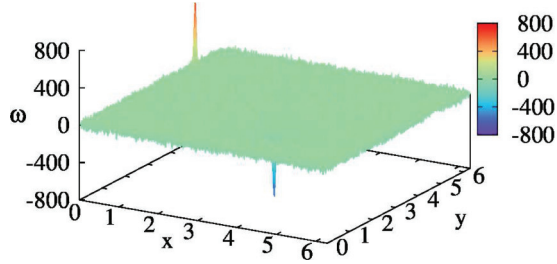
FIG. 4. (Color online) Vorticity field in physical space at $t = 300$ ($\sim 40 T_L$) in AR1.

of their vorticity grows in time after that, while the sizes of them remain comparable with the forcing scale ($\sim 2\pi / k_f$).

This difference in physical space reveals that the mechanism of the external forcing process has a strong influence on the vorticity field at least after the quasi steady state. Even when the capital numerical parameters are fixed, a completely different vorticity field can be obtained if the forcing process is changed.

The coherent structure observed in AR1 is consistent with the results in Refs. [18,20], in which the condensation process was first studied numerically in detail with a small-scale white-in-time Gaussian random forcing and the eighth-order hyperviscosity: The numerical setting is almost the same with AR1. Similar results are also observed in Ref. [33], in which energy condensation in two-dimensional turbulence is investigated with a band-limited stochastic forcing with fixed amplitude and random phase. As stated in Ref. [33], time growth of the maximum value of vorticity in AR1 is proportional to $\sqrt{t}$ in late simulation time ($t \gtrsim 50 T_L$).

At the end of the simulation time ($t \sim 60 T_L$), we calculate the background vorticity field in AR1 filtering out two coherent vortices in physical space as follows: (i) We prepare the function $g(\boldsymbol{x}) = \sum_{i=1}^{N_\Omega} \exp\left(-(\boldsymbol{x} - \boldsymbol{c}_i)^2 / 2\sigma^2\right)$, where N_Ω ($=2$) is the number of the coherent vortices, $\boldsymbol{c}_i$ the center position of i-th coherent vortex, and σ is fixed at the forcing scale $2\pi / k_f$. (ii) The background vorticity field is calculated as $\omega(\boldsymbol{x}) - g(\boldsymbol{x})\omega(\boldsymbol{x})$, where $\omega(\boldsymbol{x})$ is the original vorticity field. After this filtering, we return to Fourier space and calculate the energy spectrum of it. It is found that the energy spectrum of the background vorticity field shows k^{-1} scaling in the intermediate scale range. This result is also consistent with that in [33].
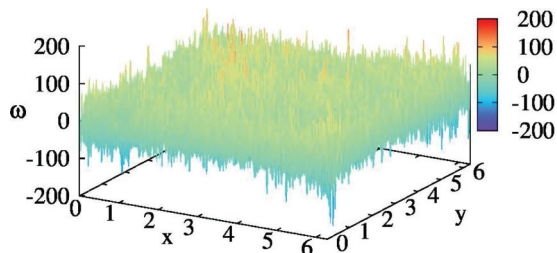

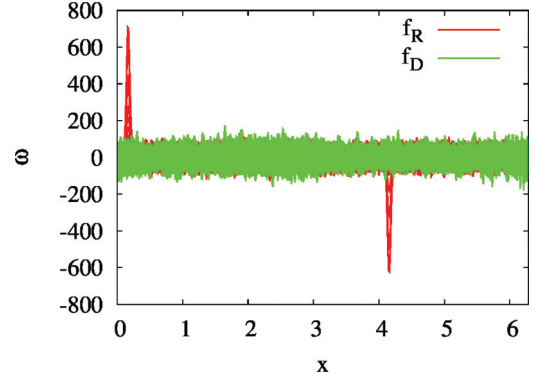FIG. 5. (Color online) Vorticity field in physical space at $t = 300$ ($\sim 40 T_L$) in AD1.

FIG. 6. (Color online) Side view of Fig. 4(f_R) and Fig. 5(f_D).

B. With the first-order hypodrag term

To attain a statistically stationary state, the first-order hypodrag term [$q = 1$ in Eq. (1)] is added as an energy sink at large scales. Time evolution of the total kinetic energy is shown in Fig. 7 for $d = 0.0, 0.2, 2.0,$ and 10.0 in both cases, f_R and f_D. These simulations correspond to AR1, BR1, BR2, BR6, AD1, BD1, BD2, and BD3 in Table I. Data for $d = 0$ (AR1 and AD1) are the same as those in Fig. 1. Since the influence of the first-order hypodrag term diminishes at high wave numbers, the effect of it is negligible at the beginning of calculation and the quasi steady state is also observed even in these cases. As the energy peak wave number k_p goes down to a lower wave number, the drag effect is intensified mainly around k_p and the total drag effect grows in time. Eventually, k_p is stabilized at a certain wave number ($\sim 2.7 k_d$), where k_d is the drag wave number defined as $(d^3 / \varepsilon_{\mathrm{tr}})^{1/(2+6q)}$. Up to this simulation time ($\lesssim 3 T_L$), the difference in the results of f_R and f_D is hardly seen when the same numerical parameters are used. Moreover, when a sufficiently large drag coefficient is set, no distinct difference is observed between the results of f_R and f_D throughout the entire simulation.

The statistically stationary state is shortly subsequent to the quasi steady state when f_D is used or when a sufficiently large drag coefficient is set as illustrated in Fig. 7. In these stationary states (in BR6, BD1, BD2, and BD3), statistical
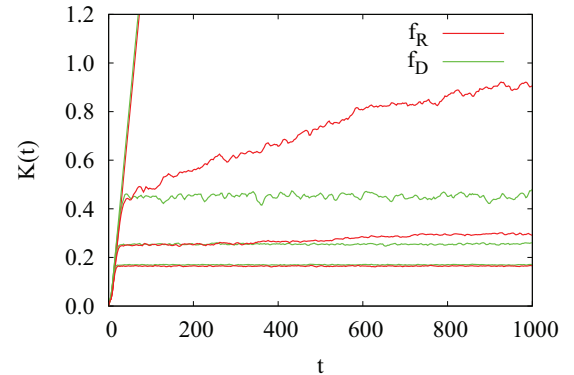

FIG. 7. (Color online) Time evolution of total kinetic energy for four drag coefficients, $d = 0, 0.2, 2.0,$ and 10 (from top to bottom) with f_R (AR1, BR1, BR2, and BR6) and f_D (AD1, BD1, BD2, and BD3). Note the overlaps between AR1 and AD1 and between BR6 and BD3. Time scale $T_L (\equiv \varepsilon_{\mathrm{in}}^{-1/3} (2\pi)^{2/3})$ is about 7.3 in all cases.
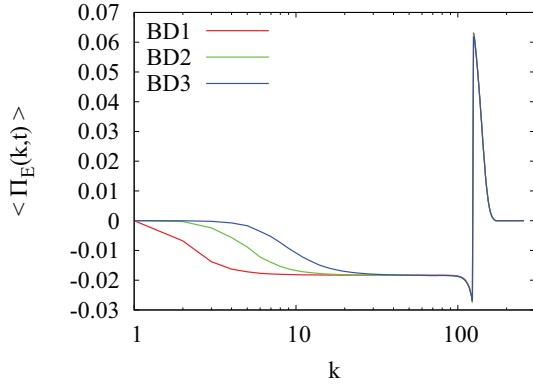
FIG. 8. (Color online) Long-time averaged energy flux functions in the statistically stationary state in BD1, BD2, and BD3 (from left to right); $d = 0.2, 2.0$, and 10 with f_D.

FIG. 10. (Color online) Long-time averaged energy spectra in statistically stationary state in BD1, BD2, and BD3 (from top left to bottom right); $d = 0.2, 2.0$, and 10 with f_D. Inset is a compensated plot; $\langle E(k,t)\rangle \varepsilon_{tr}^{-2/3} k^{5/3}$ vs k. Here, $\langle \cdot \rangle$ denotes long-time average.

features such as the energy spectrum and the energy flux function in adequately small scales [$k > k_p$ ($\sim 2.7 k_d$)] are almost the same with those in quasi steady state in the simulations AR1 and AD1 (shown in the previous Sec. III A). The long-time averaged energy flux function gives a constant value ε_{tr} (~ 0.018) in the intermediate scale range (see Fig. 8 and Fig. 9) and the $k^{-5/3}$ scaling law is clearly observed in the long-time averaged energy spectrum for this scale range (see Fig. 10 and Fig. 11). The Kolmogorov constant C_K evaluated from these results are comparable with the estimated value, 6.5 ± 1, in the laboratory experiment [41] which has attained a relatively wide inertial subrange. This value is also consistent with the previous numerical studies. These results apparently imply that Kolmogorov's phenomenology can also prevail in statistically stationary two-dimensional turbulence with a large-scale drag term.

However, when f_R is used and a small drag coefficient is set, the total kinetic energy gradually grows after the quasi steady state as demonstrated with simulations BR1 and BR2 in Fig. 7. In this second growth process, several strong coherent vortices as illustrated in Fig. 12 emerge and the intensity of them increases. A bulge in the energy spectrum also appears and increases in the intermediate scale range in this time region, which destroys the $k^{-5/3}$ scaling. After this long-term second
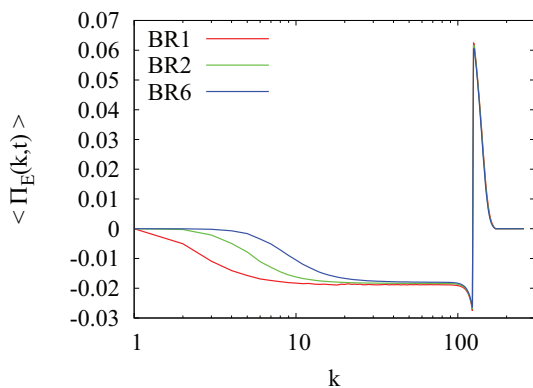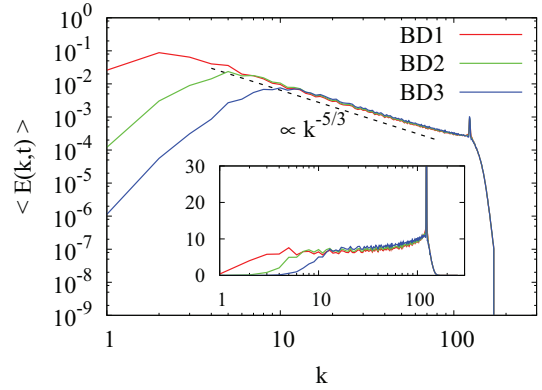
growth process, a statistically stationary state is eventually attained even in these cases.

The long-time averaged energy flux functions and the energy spectra in such statistically stationary states (in BR1 and BR2) are shown in Fig. 9 and Fig. 11, respectively. From the comparison between Fig. 8 and Fig. 9, it is obvious that the long-time averaged energy flux function depends little on the type of forcing process. On the other hand, when only f_R is used, a spectral bulge is formed in the energy spectrum for a small drag coefficient. The spectral bulge is more intense for lower drag coefficient and the $k^{-5/3}$ scaling is apparently destroyed. Even when the spectral bulge is formed, the energy peak wave number k_p stays at about $2.7 k_d$, where k_p is stabilized at the end of the quasi steady state. The linear relationship between k_p and k_d is also pointed out in the previous studies [24,44].

In such statistically stationary states where the spectral bulge is formed in the energy spectrum, several strong coherent vortices with almost the same intensity are observed in physical space, as shown in Fig. 12 and Fig. 14. The intensity of these coherent vortices fluctuates little in time. This value depends on the drag coefficient; it is more intense for small drag

FIG. 9. (Color online) Long-time averaged energy flux functions in the statistically stationary state in BR1, BR2, and BR6 (from left to right); $d = 0.2, 2.0$, and 10 with f_R.
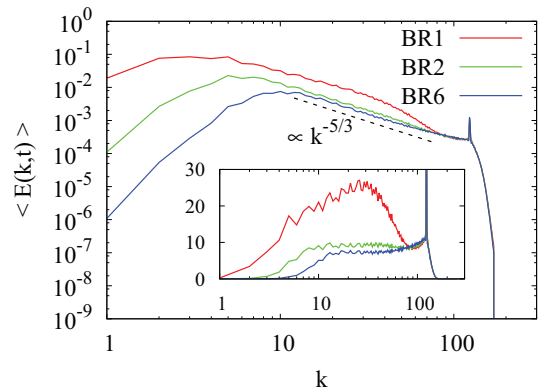

FIG. 11. (Color online) Long-time averaged energy spectra in statistically stationary state in BR1, BR2, and BR6 (from top left to bottom right); $d = 0.2, 2.0$, and 10 with f_R. Inset is a compensated plot; $\langle E(k,t)\rangle \varepsilon_{tr}^{-2/3} k^{5/3}$ vs k.
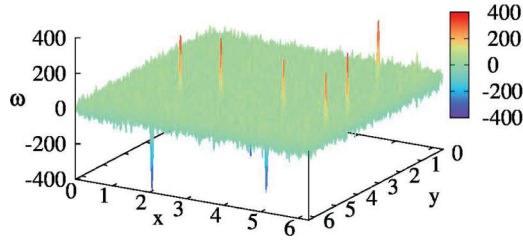
FIG. 12. (Color online) Snapshot of vorticity field in statistically stationary state of calculation BR1.

coefficient. The size of these coherent vortices are comparable with the forcing scale ($2\pi/k_f$), which is similar to the dipole coherent vortices seen in Sec. III A (see Fig. 6). These coherent vortices are not observed in the f_D cases and in the f_R cases with sufficiently large drag coefficients. Vorticity fields in these cases are structureless, as illustrated in Fig. 13 and Fig. 14.

To see the relation between the strong coherent vortices and the spectral bulge, we filter out the strong coherent vortices in an instantaneous vorticity field in statistically stationary state. The filtering method is the same as used in Sec. III A. In the energy spectrum of these remaining fluctuations, the $k^{-5/3}$ scaling is observed as repeatedly reported in the previous study [20,31,37]. This energy spectrum is almost the same as that of the simulation in which f_D and the same numerical parameters are used. It is natural to think that the departure from the $k^{-5/3}$ scaling comes from the formation of strong coherent vortices after the quasi steady state. Note that the k^{-1} scaling is obtained in the intermediate scale range when the dipole coherent vortices are filtered out in the previous Sec. III A. Thus the difference between the coherent vortices in this subsection and the dipole vortices is in the energy spectrum of the background field. The similarities are that both are formed after the quasi steady state and the sizes of them are comparable.

Strong coherent vortices are also observed in simulations CR1, CR2, CR3, CR4, DR1, DR2, DR3, DR4, DR5, and DR6 at higher spatial resolution. They are formed only when f_R and an insufficiently small drag coefficient are used. Radii of coherent vortices are comparable with the forcing scale in all simulations if they are formed. More coherent vortices are observed for higher forcing wave numbers at higher spatial resolutions. Each intensity of strong coherent vortices in statistically stationary state is at a comparable level around the maximum vorticity in each simulation as illustrated in Fig. 14. The maximum vorticity highly depends on the numerical parameters such as k_f and d.
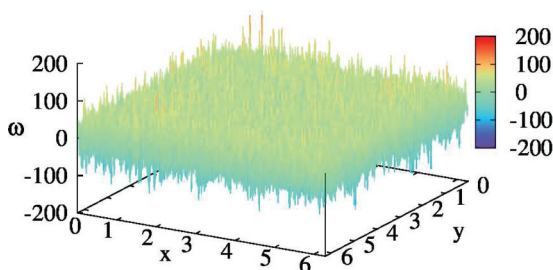

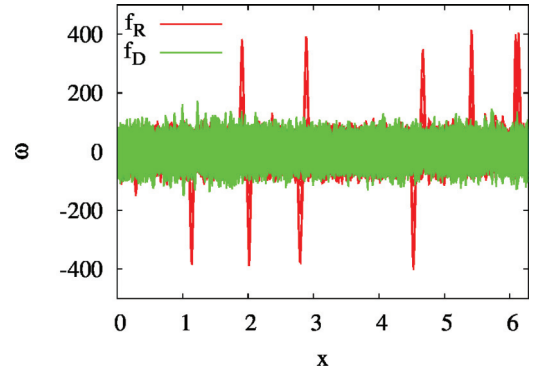FIG. 13. (Color online) Snapshot of vorticity field in statistically stationary state of calculation BD1.

FIG. 14. (Color online) Side view of Fig. 12(f_R) and Fig. 13(f_D).

To investigate the relation between the strong coherent vortices and the numerical parameters, we plot the maximum absolute value of vorticity normalized with the root-mean-square vorticity ($|\omega|_{\max}/\omega_{\mathrm{rms}}$) in a statistically stationary state against the infrared Reynolds number Re_d, defined as k_f/k_d according to Ref. [37], in Fig. 15. All the data for f_R with $q = 1$ at the resolution 512^2, 1024^2, and 2048^2 are shown in Fig. 15. Obviously there is a critical point around $\mathrm{Re}_d \sim 40$ and these data give a single curve $a_1(\mathrm{Re}_d - b_1)^{1/2} + 5$ for $\mathrm{Re}_d \gtrsim 40$, with $(a_1, b_1) = (3.1, 41)$, as if the supercritical (pitchfork) bifurcation might occur. This result suggests that not k_d but Re_d is a key factor for formation of strong coherent vortices. Note that the infrared region $[1, k_d]$ is enlarged twice and four times for the same Re_d when the resolution gets higher from 512^2 to 1024^2 and 2048^2, respectively. Thus, the shortage of spectral modes in the infrared region is not the cause of the formation of strong coherent vortices. That is, strong coherent vortices are not due to the finite-size effect. When f_R is used with $q = 1$, the spectral bulge is also observed for $\mathrm{Re}_d \gtrsim 40$. It gets to be more distinguishable as Re_d increases.

These results imply that a wide $k^{-5/3}$ scaling range cannot be observed when f_R is adopted, while a wide inertial subrange can be easily attained when f_D is used. To check this, we employ the maximum spatial resolution 4096^2 in this study
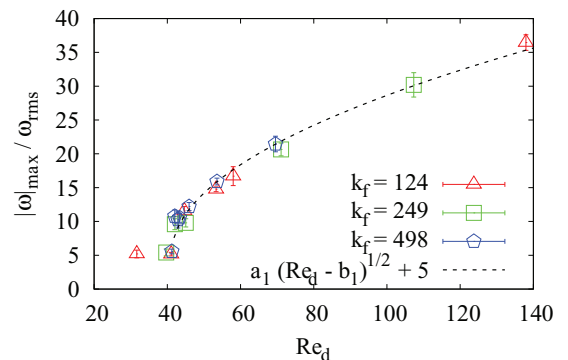

FIG. 15. (Color online) Maximum absolute value of vorticity normalized by root-mean-square vorticity in a statistically stationary state vs the infrared Reynolds number Re_d when f_R is employed, $k_f = 124, 249$, and 498, and $q = 1$. Error bars show each of maximum and minimum values in several realizations. These data can be fitted onto a single curve $a_1(\mathrm{Re}_d - b_1)^{1/2} + 5$ with $(a_1, b_1) = (3.1, 41)$ for $\mathrm{Re}_d \gtrsim 40$.
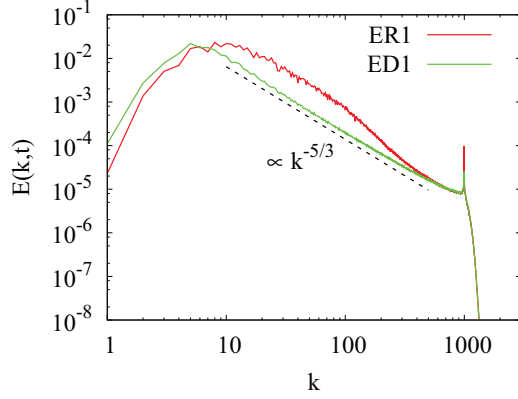
FIG. 16. (Color online) Instantaneous energy spectrum when the statistically stationary state is nearly attained in ER1 (upper) and long-time averaged energy spectrum in stationary state in ED1 (lower).

in ER1 and ED1. In these simulations, the forcing wave number is shifted to a higher wave number in proportion to the maximum wave number. Both the energy input rate $\varepsilon_{\mathrm{in}}$ and the energy transfer rate $\varepsilon_{\mathrm{tr}}$ are also fixed as in the previous cases. The results are what we expected; strong coherent vortices and a spectral bulge, which destroys the $k^{-5/3}$ scaling, are observed for f_R, while the structureless vorticity field with a relatively wide $k^{-5/3}$ scaling range is attained for f_D. The comparison of the instantaneous energy spectrum when the statistically stationary state is nearly attained in ER1 with the long-time averaged energy spectrum in stationary state in ED1 is illustrated in Fig. 16. Because of a high computational cost to trace all the energy growing processes after the quasi steady state, we stop the calculation of ER1 when the stationary state is nearly obtained.

At the end of the simulation ER1, we evaluate the maximum absolute value of the vorticity normalized with the root-mean-square vorticity ($|\omega|_{\mathrm{max}}/\omega_{\mathrm{rms}}$) and add it to the previous data in Fig. 17. This value is much smaller than the estimated value from the fitting function $a_1(\mathrm{Re}_d - b_1)^{1/2} + 5$, where $(a_1, b_1) = (3.1, 41)$, from the previous data. Judging from the little growth

of this value in final stage, this gap would not be made up for even if the calculation of ER1 continued.

If the coherent vortices in this subsection have something to do with the dipole coherent structures mentioned in the previous Sec. III A, the $\sqrt{t}$ growth of the intensity of the coherent vortices may be prevented by the drag term. Since the time scale τ_d at the drag scale $1/k_d$ is estimated as $\tau_d \sim \varepsilon_{\mathrm{tr}}^{-1/3} k_d^{-2/3}$, the intensity of the coherent vortices $|\omega|_{\mathrm{max}}/\omega_{\mathrm{rms}}$ may depend on $\sqrt{\tau_d} \sim \varepsilon_{\mathrm{tr}}^{-1/6} k_d^{-1/3} \sim \mathrm{Re}_d^{1/3}$. Here $\mathrm{Re}_d = k_f/k_d$. Thus, we also fit the previous data with the function $a_2(\mathrm{Re}_d - b_2)^{1/3} + 5$ and evaluate (a_2, b_2) as (4.7,41). However, the estimated value from this fitting curve is much smaller than the calculated value at the end of the simulation ER1, as shown in Fig. 17. While the growth of $|\omega|_{\mathrm{max}}/\omega_{\mathrm{rms}}$ with Re_d near the critical point Re_d^c seems to be expressed with $a_1(\mathrm{Re}_d - \mathrm{Re}_d^c)^{1/2} + 5$, we are not sure how $|\omega|_{\mathrm{max}}/\omega_{\mathrm{rms}}$ depends on Re_d at much higher Re_d. Even so, we expect that the coherent vortices would emerge and destroy the $k^{-5/3}$ scaling law for high Re_d when f_R is adopted. On the other hand, much wider inertial subrange would be attained when f_D is employed.

C. Combination of two types of forcing

To bridge a gap between the results of f_R and f_D, we examine some cases of the combination of both two types of forcing process. Here the random forcing ratio r_{RF} to the total forcing is defined by $\varepsilon_{\mathrm{in}}^R/\varepsilon_{\mathrm{in}}$, where $\varepsilon_{\mathrm{in}}^R$ and $\varepsilon_{\mathrm{in}}^D$ are energy input rates for f_R and f_D, respectively. In the following, the total energy input rate $\varepsilon_{\mathrm{in}} = \varepsilon_{\mathrm{in}}^R + \varepsilon_{\mathrm{in}}^D$ is fixed. We carried out simulations changing r_{RF} with using the parameters of BR1 and BR2 in Table I. The infrared Reynolds number Re_d in BR1 and BR2 are approximately 137 and 58, respectively. In Fig. 18, $|\omega|_{\mathrm{max}}/\omega_{\mathrm{rms}}$ in each statistically stationary state is plotted against r_{RF}. The results of the simulations BR6 and BD3, which correspond to $r_{\mathrm{RF}} = 1$ and 0 when $\mathrm{Re}_d = 32$, are also shown in this figure. At a large and fixed value of Re_d such that the coherent vortices are formed in the case of $r_{\mathrm{RF}} = 1$, the coherent vortices also emerge and destroy the $k^{-5/3}$ scaling law if r_{RF} is relatively close to 1. Decreasing r_{RF}
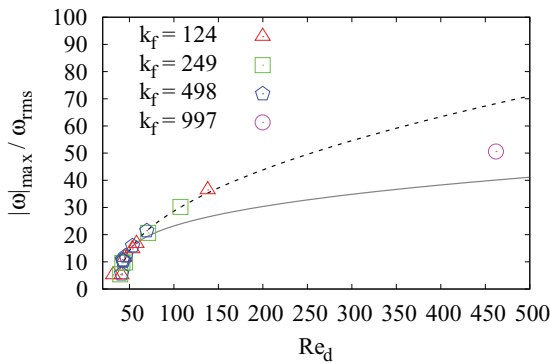

FIG. 17. (Color online) Maximum absolute value of vorticity normalized by root-mean-square vorticity vs the infrared Reynolds number Re_d when f_R is employed, $k_f = 124, 249, 498,$ and 997(ER1), and $q = 1$. Fitting lines for $k_f/k_d \gtrsim 40$, $a_1(\mathrm{Re}_d - b_1)^{1/2} + 5$ (dotted black upper line), and $a_2(\mathrm{Re}_d - b_2)^{1/3} + 5$ (solid gray lower line) are estimated with the data for $k_f = 124, 249,$ and 498, where $(a_1, b_1) = (3.1, 41)$ and $(a_2, b_2) = (4.7, 41)$.
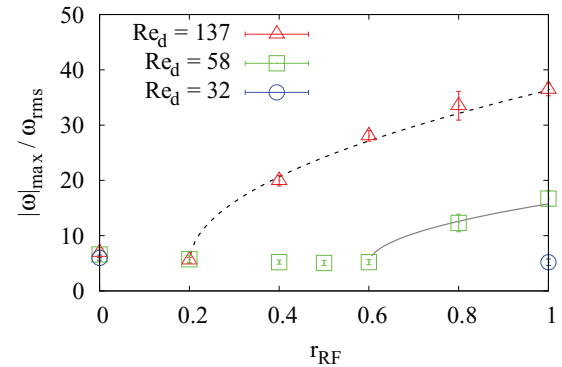

FIG. 18. (Color online) Maximum absolute value of vorticity normalized by root-mean-square vorticity in statistically stationary state as a function of the random forcing ratio r_{RF} when $\mathrm{Re}_d = 137$, 58, and 32. Error bars show each of maximum and minimum values in several realizations. Dotted black upper line is $35(r_{\mathrm{RF}} - 0.2)^{1/2} + 5$ and solid gray lower line is $17(r_{\mathrm{RF}} - 0.6)^{1/2} + 5$.
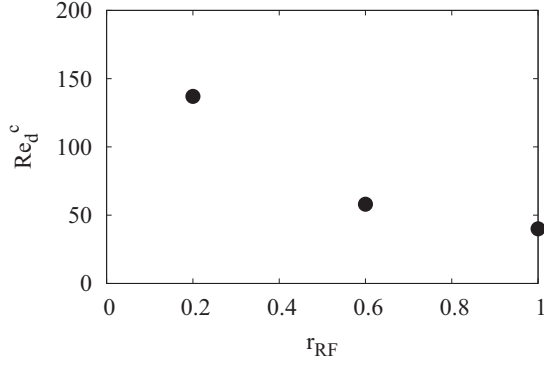
FIG. 19. Roughly estimated critical infrared Reynolds number Re_d^c against the random forcing ratio r_{RF}.

TABLE II. Numerical settings in simulations LR1 and LD1.

Name	N^2	f	k_f	ε_{in}	h	ν	q	d
LR1	2048^2	f_R	485	0.00016	8	2.651×10^{-44}	2	277.103
LD1	2048^2	f_D	485	0.00016	8	2.651×10^{-44}	2	277.103

to a critical value r_{RF}^c, which depends on the fixed value of Re_d, the intensity $|\omega|_{max}/\omega_{rms}$ also decreases. This behavior can be expressed with the function $\alpha(r_{RF} - r_{RF}^c)^{1/2} + 5$, where (α, r_{RF}^c) is $(35, 0.2)$ when $Re_d = 137$ and $(17, 0.6)$ when $Re_d = 58$ as shown in Fig. 18.

From these results, the critical infrared Reynolds numbers Re_d^c when $r_{RF} = 0.2$ and 0.6 are roughly estimated to be 137 and 58, respectively. As shown in Fig. 15, $Re_d^c \sim 40$ when $r_{RF} = 1$. This dependence of Re_d^c on r_{RF} is schematically shown in Fig. 19. From the result of ED1, Re_d^c is at least over 462 when $r_{RF} = 0$, although we expect it to be infinite. It is obvious that including even a small fraction of the random component to the forcing process can drastically change the vorticity field and destroy the $k^{-5/3}$ scaling law when Re_d is high.

D. Effect of the order of hypodrag term

Finally, we briefly examine the effect of the order q of hypodrag term. It is claimed in Ref. [22] that employing the appropriate large-scale drag formulation is important to obtain the statistically stationary turbulent flow field that is structureless and holds phenomenological statistical laws, such as the $-5/3$ energy spectrum and the constant energy flux function in the intermediate scale range. In fact, such a flow field is obtained in Ref. [22] by using a specially devised large-scale drag and a small-scale white-in-time Gaussian random forcing. In our direct numerical simulations, such an ideal inverse energy cascade flow field is obtained just with the first-order hypodrag term. Nevertheless, we test influence on the statistical features of this type of drag term by varying its inverse-Laplacian order q.

We carried out simulations FR1, FR2, FD1, FD2, GR1, GR2, GD1, HR1, HR2, HR3, HD1, ID1, JR1, JR2, JD1, and KD1 in Table I employing $q = 0, 2$, and 8. Strong coherent vortices are observed only in the simulations GR1, HR1, HR2, and JR1. The results are quite similar to those with $q = 1$: (i) Both the energy spectrum and the energy flux function are consistent with Kolmogorov's phenomenology in the inverse energy cascade range and the vorticity field is structureless when f_D is adopted. (ii) Those also hold for the case of f_R only when the infrared Reynolds number Re_d is low. (iii) Strong coherent vortices and a spectral bulge are formed when f^R is used at high Re_d. Note that the constant energy flux

range is narrow when $q = 0$ as usual [23,24], since the linear drag ($q = 0$) affects all scales uniformly as pointed out in Ref. [25]. Strong coherent vortices cannot be observed at the 512^2 resolution when $q = 0$, while they are seen in GR1 at the resolution of 2048^2.

The analytical form in the drag range of the energy spectrum depends on q and the large-scale bottleneck effect gets to be prominent for large q. The spectral bump in the energy spectrum is formed in the vicinity of k_p for large q as predicted with a closure model in Ref. [45]. It is observed for both types of forcing process. This effect, however, does not change the $k^{-5/3}$ scaling in the inertial subrange but just reduces the width of the $k^{-5/3}$ scaling range. The critical infrared Reynolds number Re_d^c for f_R also depends on q; small Re_d^c is evaluated for large q.

To see the results in another numerical setting, we also reproduce RUN3 in Ref. [34], where a relatively wide $k^{-5/3}$ scaling range is attained with f_D at the resolution of 2048^2. The numerical parameters of this simulation LD1 is shown in Table II. Clear $k^{-5/3}$ scaling is observed over one decade as in Ref. [34], with the inverse-cascade strength $\varepsilon_{tr}/\varepsilon_{in}$ is approximately 0.30. We then replace the forcing process by f_R in the simulation LR1 in Table II. The spectral bulge and coherent vortices, which are never seen in LD1, are formed and the $k^{-5/3}$ scaling is destroyed, as expected. From these results, we infer that it may be impossible to have a wide $k^{-5/3}$ scaling range when f_R is adopted.

IV. DISCUSSION AND CONCLUSIONS

Our results show that the $k^{-5/3}$ scaling law of the inertial subrange in the inverse energy cascade range is sensitive to not only the numerical parameters but also the mechanism (deterministic or random) of the forcing process. This sensitivity is traced to the formation of strong coherent vortices. These coherent vortices have been observed in many preceding numerical works [20–22,24,25,31,37,39]. It has also been repeatedly pointed out [20,21,31,37] that, even in the cases where the strong coherent vortices destroy the scaling law, once they are filtered out, the $k^{-5/3}$ scaling can be observed in the energy spectrum of the background vorticity field.

In this study, we employed two types of forcing, the random forcing f_R and the deterministic forcing f_D, and found that strong coherent vortices are formed only when f_R is adopted. The energy spectrum of the background field in these cases is almost the same as that of the entire flow field when f_D is substituted for f_R, in which the $k^{-5/3}$ scaling law is clearly observed. These observations lead a following picture: The inverse energy cascade turbulent flow field with deviation from the $k^{-5/3}$ energy spectrum can be decomposed to the coherent vortices and the background field; the former causes the deviation and the latter has the $k^{-5/3}$ energy spectrum. In spite

of the discrepancy of the energy spectrum, the universality of the inverse energy cascade phenomenology holds for the latter in fact. Formation mechanism of such coherent vortices will shed some light on universality of the inverse energy cascade state.

To characterize the coherent vortices, a parameter $|\omega|_{\max}/\omega_{\rm rms}$ is introduced in this study, because the strong coherent vortices, once they emerge, are long-lived and of the same size in general. It is found that this parameter grows like an order parameter in the case of a transition phenomenon with increase in the infrared Reynolds number $\mathrm{Re}_d (\equiv k_f/k_d)$ when f_R is adopted. With this parameter, we can detect more precisely when the coherent vortices are formed in a series of numerical simulations. Taking advantage of this methodology, we revealed that the finite-size effect is not the cause of the formation of strong coherent vortices comparing the results at different resolutions. Strong coherent vortices are formed when f_R is used and Re_d exceeds a critical value. This is the case at least when the order q of hypodrag term is $0, 1, 2,$ or 8. These results imply that a wide $k^{-5/3}$ scaling range would never be observed with f^R.

When the deterministic forcing f_D is adopted, strong coherent vortices are hardly seen and the results are consistent with Kolmogorov's phenomenology even when $\mathrm{Re}_d = 462$ at the highest spatial resolution 4096^2 in this study. This suggests that the inertial subrange can be extended with no limit like in the case of three-dimensional homogeneous isotropic turbulence. We have verified that the $k^{-5/3}$ energy spectrum does not depend on the order q of hypodrag term, even though the scaling range is shortened for large q by the large-scale bottleneck effect where the spectral bump is formed in the vicinity of the energy peak wave number.

From the results of simulations with the combination of both types of forcing processes with $q = 1$, it is also found that even a small fraction of the random forcing process can cause the formation of strong coherent vortices and destroy the $k^{-5/3}$ scaling law when Re_d is high. We currently do not have an explanation why only the simulation with f_D can be free from the coherent vortices and completely consistent with the KLB theory.

Here it is tempting to ask whether the strong coherent vortices, which are repeatedly observed in many numerical studies with various settings, can be described by a unified manner. Our opinion is pessimistic for the following reason. In our results, the sizes of strong coherent vortices are almost the same, which is comparable with the forcing scale. This size

distribution of strong coherent vortices seems to be different from that in the previous results such as shown in Ref. [21]. The growth of the vorticity is due to the forcing because the nonlinear term in the two-dimensional Navier-Stokes equations conserves the vorticity. Thus, we expect that the formation of the strong coherent vortices as follows: First, a small coherent bell-shaped vortical structure emerges via the nonlinear effect, and then its amplitude grows by the forcing and, finally, is saturated by the drag. In this process, energy may be transferred nonlocally to large scales. This expected formation process of strong coherent vortices is probably not a general phenomenon.

In this study, we restrict both the inverse-cascade strength $\varepsilon_{\rm tr}/\varepsilon_{\rm in}$ and the ratio $k_{\max}/k_f$ to low values, where $k_{\max}$ is the maximum wave number. Judging from the results in Refs. [9,20,31,37,39], this confinement on the parameter space may have a positive effect on avoiding the formation of coherent vortices. Tran [9] has shown that, even with the deterministic forcing process similar to f_D, the $k^{-5/3}$ scaling is destroyed when $\varepsilon_{\rm tr}/\varepsilon_{\rm in}$ is raised. It is also shown in Ref. [31] that strong coherent vortices are formed and destroy the $k^{-5/3}$ scaling even in quasi steady state when $k_{\max}/k_f > 16$. Raising $\epsilon_{\rm tr}/\epsilon_{\rm in}$ or $k_{\max}/k_f$ means the elongation of the dissipation-free spectral range smaller than the forcing scale. Thus we infer that a wide dissipation-free spectral range might make it easier for the strong coherent vortices to emerge.

Even when $\varepsilon_{\rm tr}/\varepsilon_{\rm in}$ and $k_{\max}/k_f$ are restricted to low values, our simulation results show that the formation of coherent vortices highly depends on the external forcing mechanism. We, therefore, conclude that a more comprehensive investigation of the formation mechanism of strong coherent vortices is required to elucidate the universality and robustness of Kolmogorov's phenomenology in two-dimensional Navier-Stokes turbulence. We will leave it for future works.

[1] R. H. Kraichnan, Phys. Fluids **10**, 1417 (1967).

[2] C. Leith, Phys. Fluids **11**, 671 (1968).

[3] G. K. Batchelor, Phys. Fluids **12**, II-233 (1969).

[4] R. Fjørtoft, Tellus **5**, 225 (1953).

[5] R. H. Kraichnan, J. Fluid Mech. **47**, 525 (1971).

[6] P. Constantin, C. Foias, and O. P. Manley, Phys. Fluids **6**, 427 (1994).

[7] G. L. Eyink, Physica D **91**, 97 (1996).

[8] C. V. Tran and T. G. Shepherd, Physica D **165**, 199 (2002).

[9] C. Tran, Physica D **191**, 137 (2004).

[10] C. V. Tran and D. G. Dritschel, J. Fluid Mech. **559**, 107 (2006).

[11] A. Alexakis and C. R. Doering, Phys. Lett. A **359**, 652 (2006).

[12] C. V. Tran, Phys. Fluids **19**, 108109 (2007).

[13] S. Kuksin and A. Shirikyan, *Mathematics of Two-Dimensional Turbulence*, Cambridge Tracts in Mathematics No. 194 (Cambridge University Press, Cambridge, 2012).

[14] P. Constantin, N. Glatt-Holtz, and V. Vicol, arXiv:1304.2022 (2013).

[15] D. K. Lilly, Phys. Fluids **12**, II-240 (1969).
[16] U. Frisch and P. L. Sulem, Phys. Fluids **27**, 1921 (1984).
[17] M. E. Maltrud and G. K. Vallis, J. Fluid Mech. **228**, 321 (1991).
[18] L. M. Smith and V. Yakhot, Phys. Rev. Lett. **71**, 352 (1993).
[19] V. Borue, Phys. Rev. Lett. **71**, 3967 (1993).
[20] L. M. Smith and V. Yakhot, J. Fluid Mech. **274**, 115 (1994).
[21] V. Borue, Phys. Rev. Lett. **72**, 1475 (1994).
[22] S. Sukoriansky, B. Galperin, and A. Chekhlov, Phys. Fluids **11**, 3043 (1999).
[23] G. Boffetta, A. Celani, and M. Vergassola, Phys. Rev. E **61**, R29 (2000).
[24] S. Danilov and D. Gurarie, Phys. Rev. E **63**, 020203 (2001).
[25] S. Danilov and D. Gurarie, Phys. Rev. E **63**, 061208 (2001).
[26] C. Pasquero and G. Falkovich, Phys. Rev. E **65**, 056305 (2002).
[27] S. Chen, R. E. Ecke, G. L. Eyink, X. Wang, and Z. Xiao, Phys. Rev. Lett. **91**, 214501 (2003).
[28] C. V. Tran and J. C. Bowman, Phys. Rev. E **69**, 036303 (2004).
[29] C. H. Bruneau and H. Kellay, Phys. Rev. E **71**, 046305 (2005).
[30] S. Chen, R. E. Ecke, G. L. Eyink, M. Rivera, M. Wan, and Z. Xiao, Phys. Rev. Lett. **96**, 084502 (2006).
[31] R. K. Scott, Phys. Rev. E **75**, 046301 (2007).
[32] G. Boffetta, J. Fluid Mech. **589**, 253 (2007).
[33] M. Chertkov, C. Connaughton, I. Kolokolov, and V. Lebedev, Phys. Rev. Lett. **99**, 084501 (2007).
[34] Z. Xiao, M. Wan, S. Chen, and G. L. Eyink, J. Fluid Mech. **619**, 1 (2009).
[35] A. Bracco and J. C. McWilliams, J. Fluid Mech. **646**, 517 (2010).
[36] G. Boffetta and S. Musacchio, Phys. Rev. E **82**, 016307 (2010).
[37] A. Vallgren, J. Fluid Mech. **667**, 463 (2011).
[38] M. M. Farazmand, N. K. R. Kevlahan, and B. Protas, J. Fluid Mech. **668**, 202 (2011).
[39] J. Fontane, D. G. Dritschel, and R. K. Scott, Phys. Fluids **25**, 015101 (2013).
[40] J. Sommeria, J. Fluid Mech. **170**, 139 (1986).
[41] J. Paret and P. Tabeling, Phys. Rev. Lett. **79**, 4162 (1997).
[42] M. A. Rutgers, Phys. Rev. Lett. **81**, 2244 (1998).
[43] T. G. Shepherd, J. Fluid Mech. **183**, 467 (1987).
[44] K. S. Smith, G. Boccaletti, C. C. Henning, I. Marinov, C. Y. Tam, I. M. Held, and G. K. Vallis, J. Fluid Mech. **469**, 13 (2002).
[45] W. Bos and J. Bertoglio, J. Turbulence **10**, 1 (2009).